Isothermal Titration Calorimetry in Nanoliter Droplets with Sub-Second Time Constants

By

Brad Lubbers

Thesis

Submitted to the Faculty of the

Graduate School of Vanderbilt University

in partial fulfillment of the requirements

for the degree of

MASTER OF SCIENCE

in

Biomedical Engineering

December, 2011

Nashville, Tennessee

Approved:

Franz Baudenbacher

Joel Tellinghuisen

ACKNOWLEDGEMENTS

I wish to thank Franz Baudenbacher for all his support and guidance of this research. I also thank my loving wife who puts up with me and has been nothing but supportive. This research would not have been possible without the funding support of NIH Grant U01AI061223 and the fostering research atmosphere provided by Vanderbilt Integrative Biosystems Research and Education (VIIBRE).

TABLE OF CONTENTS

		Page
ACKNOWLEDGEMENTS		ii
LIST OF FIGURES		v
Chapter		
I.	INTRODUCTION	1
	Specific Aims	2
II.	MANUSCRIPT: *ISOTHERMAL TITRATION CALORIMETRY IN NANOLITER DROPLETS WITH SUB-SECOND TIME CONSTANTS*	4
	Abstract	4
	Introduction	5
	Experimental Section	6
	Sensor Description	6
	Amplifier Design	7
	Sample Delivery	9
	Sample Stabilization	10
	Time Constant Measurements	12
	Sensitivity Calibration	12
	Sensor Modeling	13
	Results and Discussion	13
	Modeling	13
	Determination of Power Sensitivity	16
	Device Optimization	18
	Error	20
	Determination of Time Constant	21
	Minimum Detectable Energy	22
	Conclusions	23
	Acknowledgements	24
	References	25
III.	CONCLUSIONS AND FUTURE WORK	28
	Conclusions	28
	Future Work	28

Appendix

A. LABVIEW SIGNAL RECORDER AND INJECTION CONTROL 30

Front Panel 30
Block Diagram 31

B. MATLAB SIGNAL PROCESSING M CODE 32

heat_equations.m 32
deconvouvle.m 34

C. COMSOL FITTING AND OPTIMIZATION M CODE 37

run_fitting_5nl.m 37
comsol.m 38
run_optimization_poly.m 42

LIST OF FIGURES

Figure		Page
1.	Sensor Setup Diagram and Junction Layout	7
2.	Sensor and Amplifier Noise	8
3.	Baseline Shift Due to Sample Injection	10
4.	Baseline Shift Due to Surface Area Change	11
5.	Model Fitting	15
6.	Sensitivity and Noise Equivalent Power	17
7.	Device Optimization	20
8.	Time Constant	21
9.	Minimum Detectable Energy	23

CHAPTER I

INTRODUCTION

Essential to all chemical reactions, molecular interactions, biological processes, and in fact every event in the universe changes the enthalpy or total energy of a thermodynamic system according to the laws of thermodynamics. The change in total enthalpy can only be measured according to the first law of thermodynamics:

$$\Delta S = Q - W$$

where ΔS is the change in total energy, Q is the heat added or taken out of the system, and W is the work performed by or on the system respectively. At constant pressure and volume all changes in enthalpy result in temperature changes. The field of isothermal titration calorimetry deals with measuring this heat and characterizing reactions and processes based on it. When the change in temperature of an isolated reaction is integrated over time, the change in enthalpy due to that reaction can be determined. The more accurately that temperature can be measured, the smaller the enthalpy changes that can be detected. Similarly, the quicker the measurement system reacts to changes in temperature, the more details about the process can be elucidated.

In the interest of maximizing calorimeter performance and accessing a higher bandwidth, there is a drive towards smaller sample volumes. This maximizes sensitivity and minimizes the time constant by reducing the thermal mass of the sample and measurement system. At the same time, the sample must be well insulated from the environment to reduce the loss of heat from the sample. With the reduction of sample volumes to nanoliter levels, the possibility of single cell biological measurements become feasible. Directly measuring the energy evolved by a single

cell would allow for the measurement of previously inaccessible physiological processes. This information could provide insight into hypertrophic cardiomyopathy, cancer, and other metabolically altering disease states. It could also be used to investigate normal cellular processes with large energy signatures like muscle contraction, neurotransmitter release, and apoptosis. Small volume calorimeters could also be utilized in array formats for high throughput drug screening.

Specific Aims

In order to develop and utilize a calorimetric system sensitive enough for measuring single cell processes, several goals must be achieved:

1) Design a measurement system around a commercially available thin film infrared sensor that we already know has the potential to measure nanowatt range reaction energies. By utilizing an off-the-shelf device we reduce start up time by avoiding establishing microfabrication processes, and can focus on calibration, liquid handing, and environmental isolation of the measurement chamber.
2) Gain a clear understanding of the kinetics involved in small volume reactions. At these small volumes, evaporation, perturbation of the sample drop, and non-linear processes can have profound effects on the measurements and must be accounted for.
3) Construct a finite element heat conduction model capable of accurately predicting the outcome of these reactions to aid in our understanding and to validate our results.
4) Utilize the finite element model to design a new calorimeter tailored to nanowatt measurements. By designing a new calorimeter in the validated model, device geometries

and material properties can be selected that maximize power sensitivity and minimize the time constant.

CHAPTER II

MANUSCRIPT: *ISOTHERMAL TITRATION CALORIMETRY IN NANOLITER DROPLETS WITH SUB-SECOND TIME CONSTANTS*

By

Brad Lubbers, Franz Baudenbacher

Abstract

We reduced the reaction volume in microfabricated suspended-membrane titration calorimeters to nanoliter droplets and improved the sensitivities to below a nanowatt with time constants of around 100ms. The device performance was characterized using exothermic acid-base neutralizations and a detailed numerical model. The finite element based numerical model allowed us to determine the sensitivities within 1% and the temporal dynamics of the temperature rise in neutralization reactions as a function of droplet size. The model was used to determine the optimum calorimeter design (membrane size and thickness, junction area, and thermopile thickness) and sensitivities for sample volumes of 1 nl for silicon nitride and polymer membranes. We obtained a maximum sensitivity of 153 pW/√Hz for a 1 μm SiN membrane and 79 pW/√Hz for a 1 μm polymer membrane. The time constant of the calorimeter system was determined experimentally by using a pulsed laser to increase the temperature of nanoliter sample volumes. For a 2.5 nanoliter sample volume, we experimentally determined a noise

equivalent power of 500 pW/√Hz and a 1/e time constant of 110ms for a modified commercially available infrared sensor with a thin-film thermopile. Furthermore, we demonstrated detection of 1.4 nJ reaction energies from injection of 25 pl of 1 mM HCl into a 2.5 nl droplet of 1 mM NaOH.

Introduction

Isothermal titration microcalorimetry is one of the most powerful techniques to characterize chemical binding mechanism and biological processes through enthalpy changes at constant temperatures[1]. In a series of additions, reagent are injected into a sample volume under isothermal conditions and by integrating small temperature increases over time, as compared to the baseline temperature, reaction enthalpies are determined[2-3].

Micromachined membrane based calorimeters allow for a dramatic reduction in sample volumes and thermal mass and therefore enable measurements with very small heat capacities[4]. Combined with a sensitive thermometer relying on the Seebeck effect, these devices reach detection limits in the nanowatt range[5]. Since change in enthalpy is a nearly universal fingerprint of binding reactions and phase transitions, these devices are used in areas such as bioscience[6], biophysical chemistry[7], chemical engineering[8], drug development[9], antibody engineering[10] and cellular assays to determine cellular growths or metabolic rates[11].

Many biothermodynamic processes occur at characteristic time constants linked to intrinsic physical kinetics or metabolic/signaling activity of living cells. Of particular interest is protein binding/folding/unfolding[12], phase transitions,[4] or physiometry to determine the activity of living cells[13].

The reduction of the sample volume implies a decrease in the time constant; allowing the temporal dynamics of the chemical and biological processes become accessible. In this study we reduced the reaction volume to nanoliter droplets and utilized a membrane based calorimeter to obtain time constants on the order of 100 ms and detection of nJ reaction energies. The response time of the system depends on the location of the heat generated, the diffusion of heat in the sample volume, and the thermal coupling of the sample volume to the heat sink. To understand these different contributions, we derived a detailed finite element model to represent the data and used the model to optimize the device performance.

Experimental Section

Sensor Description

In order to measure sub-nanowatt reaction enthalpies and characterize chemical processes, very small ΔT (<100 μK) must be detected. A commercial infrared (IR) radiation sensor (S-25, Dexter Research) was evaluated for calorimetry as the manufacturer states a sensitivity of 193 V/W, a time constant (τ) of 9 ms, and a moderate thermopile resistance of 23 KΩ, which defines the noise floor of the system. Since the sensor is designed for IR detection and not for calorimetry, the stated sensitivity and τ will vary due to the presence of the sample drop and the method of calibration. The sensor consists of 20 bismuth/antimony (Bi/Sb) thermopile junctions on a suspended 1.5 μm thick silicon nitride/silicon oxide membrane. A 0.5 mm deep by 2 mm wide chamber is formed on top of the membrane by the sensor casing and is an ideal size for holding small, nanoliter sample droplets (Figure 1B).

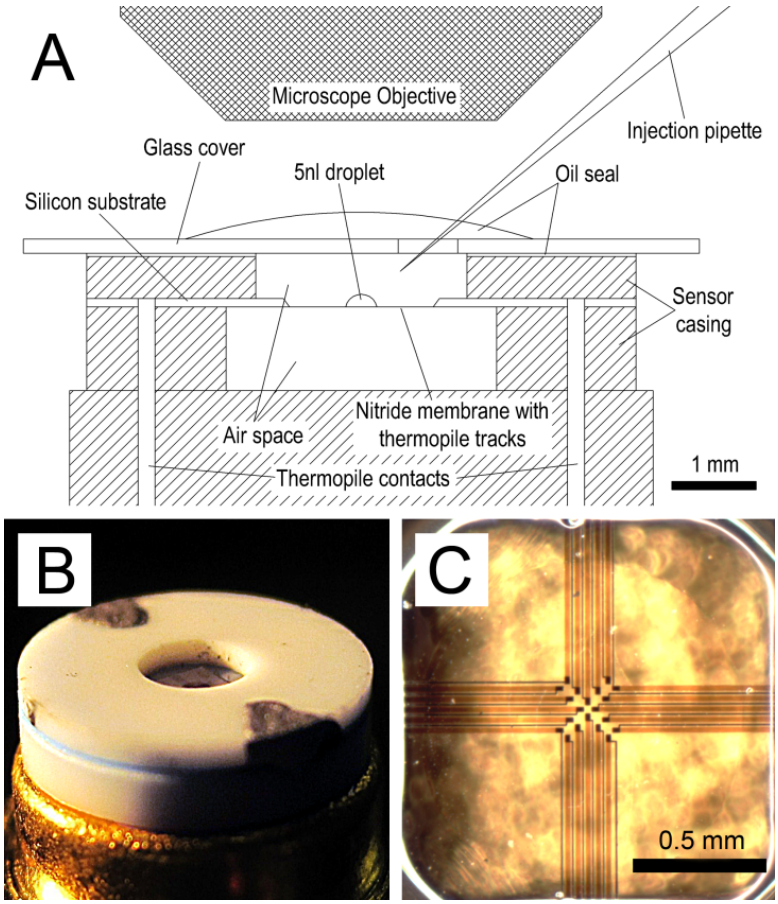

Figure 1. A) Side-view schematic of calorimeter setup showing chamber sealing with oil and sample delivery pipette. Additional shielding (not shown) around the sensor reduces thermal fluctuation noise. **B)** Angle view of sensor showing sample well in center. **C)** Top view of sensor membrane showing 20 Bi/SB thermopile junctions with an active area of 0.0625 mm^2 and sensitivity of 3600 µV/K.

Amplifier Design

The intrinsic noise of the micromachined calorimeter is dominated by the Johnson-Nyquist noise of the thermopiles and can be described by the spectral noise density:

$$V_n = \sqrt{4\,k_B T R} \qquad (1)$$

where k_B is the Boltzmann's constant, T the resistors absolute temperature, and R the resistance of the thermopile. The 23 kΩ thermopile resistance results in a noise density of 19.4 nV/√Hz. In order to operate the calorimeter close to the intrinsic noise floor, the amplifier noise should be much smaller so as not to contribute substantially to the overall noise. Since isothermal

calorimeters are typically operated near DC, the contribution of flicker or 1/f noise from the amplifier often becomes a dominating factor. Therefore, we selected a zero offset DC chopper amplifier (LMP2021, National Semiconductor) as the amplifier for our read out circuitry. Noise spectra were measured using a 3265A Dynamic Signal Analyzer (Hewlett-Packard). The noise spectrum of our amplifier is essentially white with a noise floor of 15 nV/√Hz, which leads to an overall sensor and amplifier noise of 30 nV/√Hz (Figure 2). Above 1.5 Hz, the sensor plus amplifier signal decreases due to the characteristics of the 7 Hz low pass filter.

The cutoff frequency of the amplifier depends on the thermal time constant, which in turns is a function of sample volume. At a minimum realistic sample volume of 2.5 nl we obtained a time constant of 110 ms or f_{-3dB} of 1.45 Hz. This represents the bulk time constant of the sensor and therefore we selected a cutoff frequency of 7 Hz to suppress 60 Hz line noise and reduce the Johnson noise bandwidth. The amplifier output was sampled using a National Instruments 12 bit

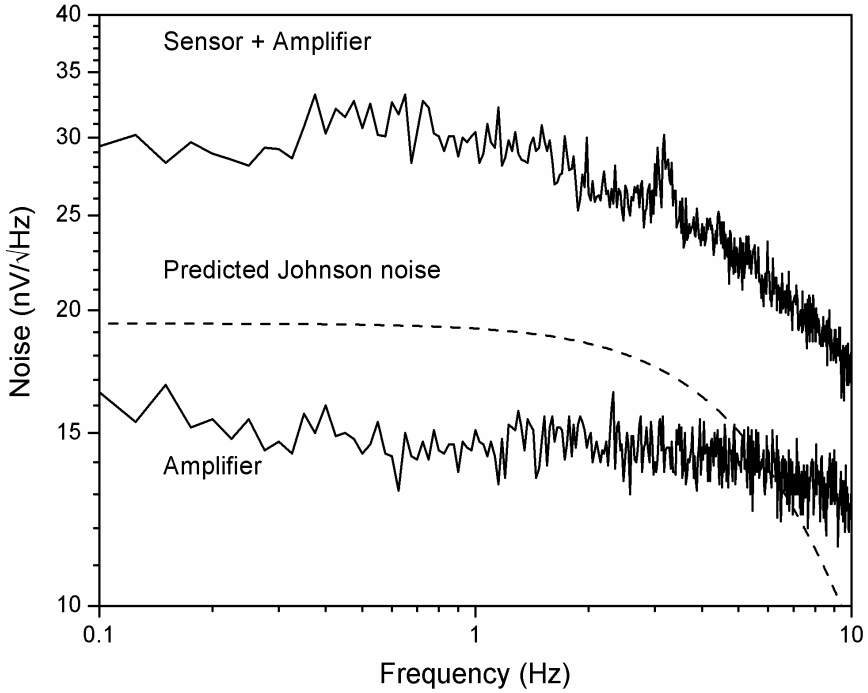

Figure 2. Noise spectral density of the amplifier, sensor, and calculated Johnson noise of the sensor, all at a 7 Hz cutoff. The combined sensor and amplifier noise is 30.1 nV in a 1 Hz bandwidth and free of 1/f noise.

PCI-6024E A/D card. Through oversampling and decimation, its effective bit count was increased to 16 and therefore the digitization noise was reduced to 7 nV/√Hz at a gain of 25,000.

All measurements were performed at room temperature (22-24 °C). During setup and measurements, the chamber of the sensor was covered by a glass cover slide with an access hole drilled for sample delivery (Figure 1A). The cover slide was sealed with mineral oil to prevent sample evaporation. Thermal fluctuations were greatly reduced by adding additional copper shielding to the sensor casing. Without the additional thermal shielding the sensor was extremely susceptible to any air drafts or changes in the ambient temperature. In addition, the grounded copper ring and a metal amplifier enclosure reduced EMF noise. The combined effects of the low noise amplifier, shielding, and filtering reduced the RMS noise to 30.1 nV in the 0-1 Hz bandwidth and the peak-to-peak noise of the system to approximately 290 nV over a 10 second window under actual experimental conditions.

Sample Delivery

Liquid sample injections were performed using a micromanipulator (MP-285, Sutter Instrument Co.) and a pressure driven injection system (PicoSpritzer II, Parker Hannifin Corp.), both controlled through LabVIEW. This allowed automated pipette placement and sample injection of sample volumes between 25 pl and 50 nl onto the sensor. Pipettes were prepared by pulling on a Flaming/Brown pipette puller (P-87, Sutter Instrument Co.) and fire polished to a 1-20 um ID using a microforge (MF-9, Narishige). Pipettes were calibrated before and after measurements by making repeated injections into a small diameter tube and measuring the total volume dispensed. In comparison to microfluidic based calorimeter devices, there is no noise contribution from the flow of reactants[14]

Sample Stabilization

Since our sample volume is a free standing nl sized droplet, evaporation is a major issue. In an unsealed sensor chamber, 2.5 nl of water would evaporate in a few seconds, so we have to stabilize the sample volume and reduce evaporation. The main strategy involved the use of a glass lid with a sealed sample injection port (Figure 1A). Since pipette access to the sensor surface was necessary for sample delivery, mineral oil was used as vapor tight seal that a micron sized delicate pipette tip could penetrate. However, sample evaporation was never completely reduced to zero and becomes critical as the sample volume is reduced[14]. For example a 5 nl water drop left on the sensor overnight would evaporate completely. This residual evaporation leads to a constant cooling flux and offsets the sample temperature slightly but measurably from the ambient temperature. The offset was integrated over the time it took for the evaporation of the droplet and was equivalent to the enthalpy of vaporization of the sample volume at the

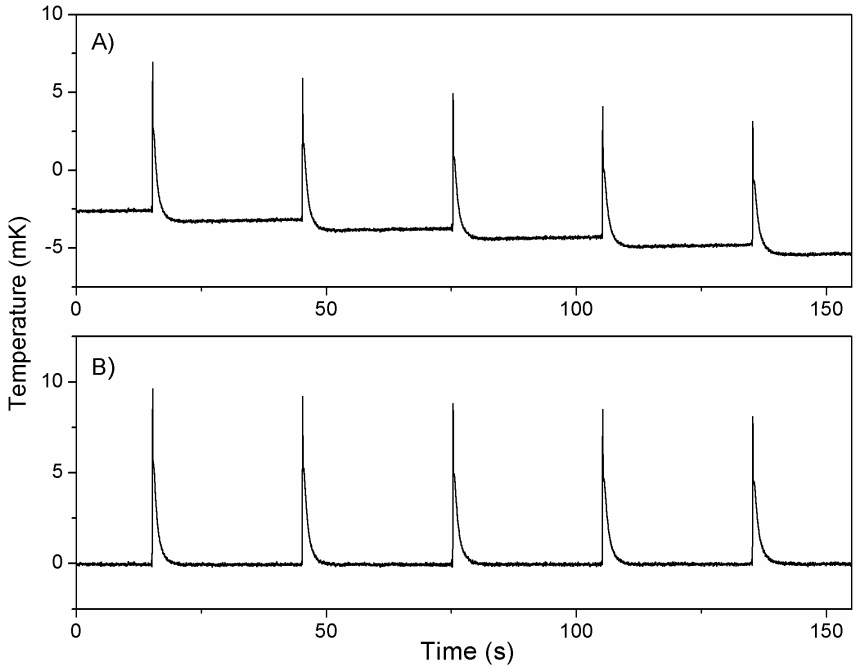

Figure 3. A series of 100 pl injections of 0.05M HCl into 2.5 nl of 0.05M NaOH obtained for calibration. A) Raw data and B) data with the baseline shift and offset corrected for.

beginning. As the evaporating droplet changes geometry or droplets are injected, the evaporative flux will be altered. Therefore, injections of liquid reagent into a sample drop results in a lower signal baseline (Figure 3). When smaller water drops were repeatedly injected to increase the base droplet, it was found that the baseline shift scaled with the change in surface area of the drop (Figure 4). Though the evaporative flux per area remains constant during an experiment, it varies between experiments due to changes in sensor sealing efficiency. In order to account for the baseline shift when determining the energy evolved in a reaction, the shift occurs instantly and can be approximated as a step function with amplitude x. When the signal is convolved with a step function of amplitude -x, the original signal can be easily recovered (Figure 3B).

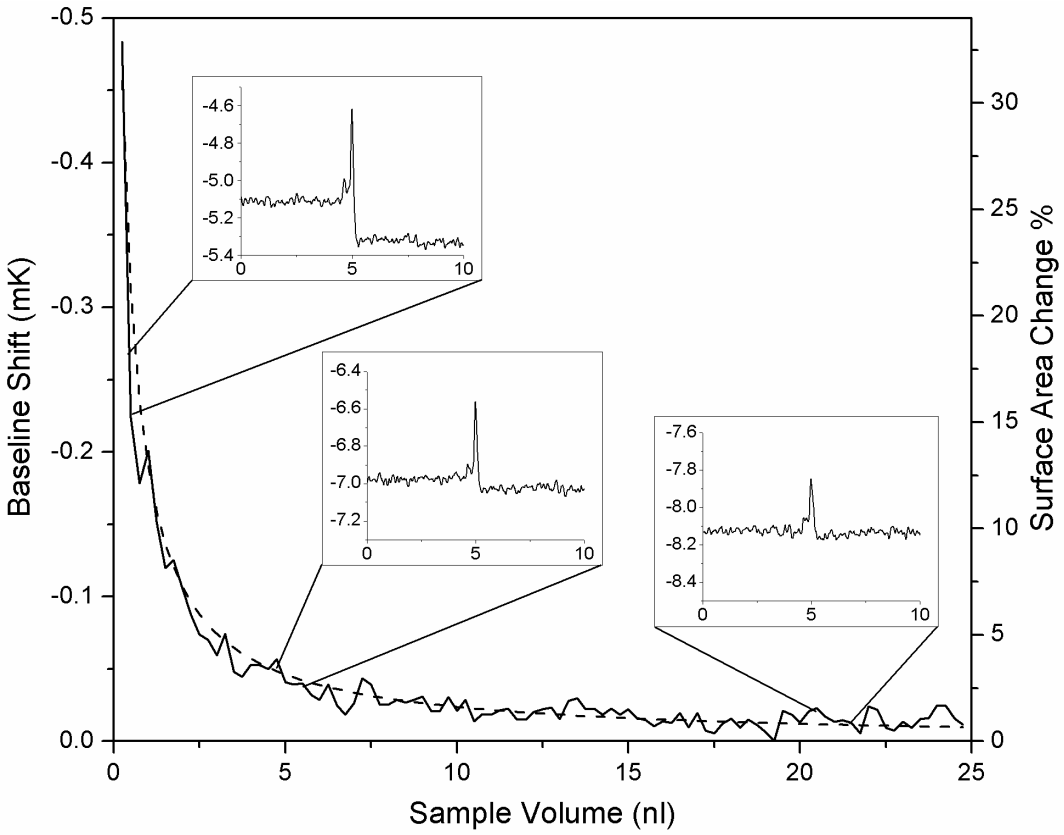

Figure 4. Shift in baseline of water droplets injected with 250 pl of additional water (inserts). The baseline shift scales with the surface area change (dashed line) of the drops due to the increased evaporative flux from the drop surface. The positive spikes during injection are due to the ΔT between the injected water and the cooled base droplet.

The evaporative sample cooling leads to a temperature difference (ΔT) between the sample volume and the injected reactants. This temperature difference causes a slight peak during any injection and the peak energy equals the specific heat of the injected sample multiplied by ΔT. The water injection peaks in Figure 4 have energies of 4.6 – 8.2 nJ, giving a calculated ΔT of 4.8 – 8.6 mK which is a realistic ΔT. We were able to eliminate, and even drive this peak negative, by holding the base drop several mK above ambient temperature using a focused laser.

Time Constant Measurements

The sensor time constant (τ) was measured at different sample volumes using a 650 nm laser as a heat source. The laser was focused through the microscope optics to a point in the center of the sensor ~100 μm wide. Starting with an empty membrane, the laser was pulsed slowly (0.1 Hz) and 1 nl of ddH_2O was repeatedly injected onto the sensor until 50 nl was reached. τ was calculated from the 1/e rise and fall time at 0-50 nl using MATLAB.

Sensitivity Calibration

Sensitivity was determined using the neutralization reaction between HCl and NaOH. Stocks of HCl and NaOH were freshly prepared in ddH_2O at concentrations of 0.01 M, 0.05 M, 0.1 M, and 0.5 M filtered with a 0.22 μm syringe filter before use. New glass pipettes were used each time to prevent contamination and tip fouling. To calibrate, a drop of NaOH between 2.5-50 nl was injected onto the sensor membrane and allowed to stabilize resulting in a flat temperature baseline. Then, a pipette containing HCl was used to inject small (0.5%-2% of base drop) volumes of HCl into the center of the NaOH drop. Identical molarity of the acid and base were used to eliminate dilution effects. The signal output was recorded in LabVIEW and then exported to MATLAB for data analysis. Sensitivity was determined by integrating the area under the curve from the exothermic reaction and dividing by the predicted reaction energy.

Sensor Modeling

In order to validate our findings and provide insights on how to optimize measurement sensitivity, a 2-D radial heat conduction model of the sensor was constructed in Comsol Multiphysics. The model included the sensor casing, glass cover, Si substrate, membrane, thermopiles, air spaces, and sample droplet. The heat origin was a sphere the same size as the injected HCl in the middle of the NaOH drop. Since some parameters (membrane thermal conductivity (G_{mem}) and total thermopile Seebeck coefficient (S_{tot})) were not provided by the sensor manufacturer, these were determined by least squares fitting of the model to experimental data. Using these parameters, sensitivity and τ were calculated in MATLAB using the Comsol data at several volumes between 0-50 nl. This model was then utilized in designing a 2nd generation calorimeter with optimized dimensions at small sample volumes for improvements in sensitivity and τ.

Results and Discussion

Modeling

The use of Comsol Multiphysics allowed for rapid modeling and the ability to least squares fit the modeling parameters to the experimental data in MATLAB. The three main parameters characterizing a calorimeter are power sensitivity (P), minimum detectable power (Pmin), and time constant (τ). They are related through the following equations:

$$P = S_{tot}/G_{tot} \quad (2)$$

where S_{tot} is the total Seebeck coefficient of the thermopiles and G_{tot} is the total thermal conductance away from the sample drop. The minimum detectable power is predicted by:

$$P_{min} = \Phi/P \quad (3)$$

where Φ is the total electronic and thermal noise of the system. The temporal response is predicted by

$$\tau = C_{tot}/G_{tot} \quad (4)$$

where C_{tot} is the total thermal mass of the sample and device. Since S_{tot} and Φ are intrinsic quantities of the device, G_{tot} and C_{tot} are the only variables dependent on the droplet size. C_{tot} can be calculated from the sample and membrane mass, however G_{tot} encompasses all heat fluxes away from the sample through the membrane, thermopiles, air, and radiation. Therefore, a numerical model of the device is required to predict G_{tot}.

Ideally, a full 3-D model would be used to encompass all device geometries. However, the thin 1.5 μm thick membrane in combination with a 2 mm wide chamber resulted in an overly complex mesh that could not be solved efficiently. Therefore, we pursued a radial 2-D model. The only feature of the sensor not radially symmetric was the thermopile traces, as can be seen in Figure 1C, so the thermal conductivity of the thermopile traces was combined into the overall conductivity of the membrane (G_{mem}). Though constant, initially the Seebeck coefficient was unknown and not provided by the device manufacturer. Based on the dimensions and resistance of the thermopile traces, it was presumed that they were made of bismuth and antimony. Bi/Sb thermopiles are reported to have thermopowers of 90-410 μV/K per junction depending on dopants and crystal orientation[15]. Even if the exact composition of the materials was known, it would still be difficult to predict their properties as these deviate from the normal bulk properties in thin films[16]. It would also be difficult to determine experimentally the thermopower of our sensor by applying a known temperature difference across the thermopile due to its small size and high sensitivity. Instead it was easier to fit the model to independent experimental

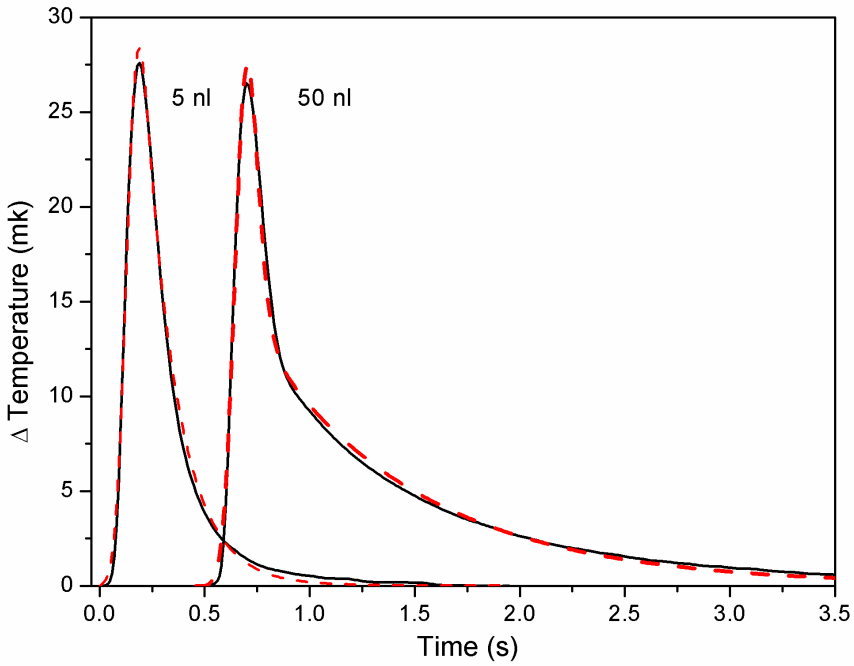

Figure 5. Exothermic acid-base neutralizations used for calibration at 5 and 50 nl. The experimental data (solid lines) are well predicted by the modeling results (dashed). 100 pl of 0.1 M HCl was injected at 0 s into 5 nl of 0.1M NaOH yielding 0.565 μJ. 500 pl of 0.1 M HCl was injected at 0.5 s into 50 nl of 0.1M NaOH yielding 2.83 μJ.

calibrations at various different sample volumes. As can be seen in Figure 5, by varying G_{mem}, S_{tot}, and the location of the heat origin, the model can be fit to the data accurately, in terms of both amplitude and temporal response. G_{mem} most directly affected τ, while S_{tot} is a scaling factor, as expected from equations 2 and 4. The residual sum of squares of the data in Figure 5 showed less than 1% error between the experimental and modeling data. The least square fitting gave similar values of G_{mem} (18.9 +/- 0.79 W/ (m •·K)) and S_{tot} (3590 +/- 260 μV/K) regardless of the sample volume or energy evolved. This high S_{tot} value combined with the low noise floor yields a temperature sensitivity of 25 μK/√Hz. This represents a threefold improvement in RMS noise compared to our previous work [5] and a 10 fold improvement in temperature resolution over microfluidic based calorimeter devices [17]. The model also showed that the location of the heat origin in the base droplet could significantly affect the results. The shoulder seen at 1.0 s in the

50 nl sample in Figure 5 varied depending on the heat origin location and disappeared when the heat origin was near the top of the sample drop. However, this reduced the curve areas and sensitivity by 30%. The effect decreased to <7% at smaller drop sizes as the volume-to-surface-area ratio of the drop decreased.

Determination of the Power Sensitivity

The acid-base neutralization injections provided a straightforward way to calibrate our sensors. Unlike calorimeters utilizing a built in heater for calibrations, our sensors are calibrated in the same fashion in which they will be used. Resistor heating on the underside of the membrane produces localized heating at the thermopile junctions and a temperature gradient throughout the sample[14]. This can lead to overestimations of sensitivity and does not take into account properties like surface area changes and finite diffusion rates that occur during reactant injections[18]. The binary reaction of HCl and NaOH was chosen for calibrations due to fast diffusion and reaction rates. When low concentration HCl is injected into an excess of equimolar concentration NaOH, the reaction occurs almost instantaneously and with very little variation between injections due to dilution of the NaOH[18]. Diffusion modeling of dilute HCl diffusion within our samples revealed that it could take up to 10 s to reach 99% uniformity. However, in all experimental cases, the reactions appeared to occur in <200 ms. This can be seen in Figure 5 where the time from the start of the injections at 0.1 s to the peaks is ~150ms. The faster than expected reaction is likely due to the turbulent flow produced during injection and the reaction completing long before concentration equilibrium was reached.

The calibration results show that a sensitivity of up to 60 V/W can be achieved by reducing the sample volume to 2.5 nl which was verified by the model results (Figure 6). In Figure 6, each triangle represents an individual injection of 0.05 M HCl into 0.05 M NaOH and each has been

corrected for baseline shift and ΔT at the time of injection. Calibrations were also performed at 0.01 M, 0.1 M, and 0.5 M to verify further the results. From this, the experimental sensitivity can be predicted empirically by:

$$P_{exp} = 88.07 \times Volume^{-0.409} \quad (5)$$

with an R^2 = 0.992 for 2.5 to 60 nl. The noise equivalent power of 0.5 nW/√Hz at 2.5 nl translates to a minimum power resolution of 1.5 nW/√Hz at a SNR of 3:1. To verify these results, model predictions of G_{tot} and S_{tot} were fed into equation 2 and the result matched well with the experimental data (Figure 6). The model revealed that G_{tot} ranged from 65 μW/K at 2.5 nl to 220 μW/K at 50 nl, with the membrane providing the main heat flow path away from the

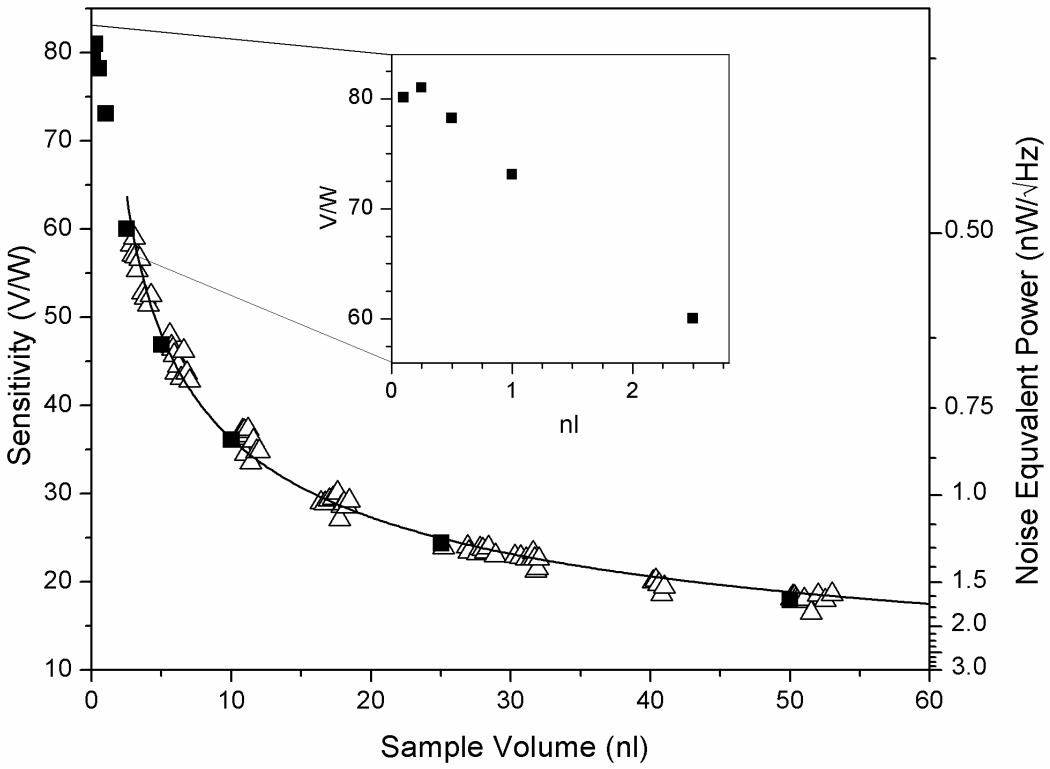

Figure 6. Experimentally determined sensitivity (Δ) determined with acid-base neutralizations. 2.5 nl is an experimental practical limit due to drop instability at small volumes. Model data (■) shows that the ultimate limit of the sensor is ~80 V/W at 0 nl sample volume. The experimentally obtained sensitivity at 2.5 nl, in conjunction with the low noise amplifier, gives an NEP of 500 pW/√Hz.

sample drop. G_{tot} increased at larger sample volumes due to the increase in surface area and the shortening of the distance between the sample and sidewalls. The near exponential increase in power sensitivity at smaller sample volumes motivated the investigation of even smaller sample volumes. Although 2.5 nl was the minimum stable droplet size in our current setup, the model was used to determine sensitivities at reduced volumes. The maximal sensitivity of 80 V/W achieved near zero volumes shows further reductions in sample volume does not led to dramatic improvements in sensitivity with our current device as would be predicted from equation 5 (Figure 6).

The calculated maximal sensitivity of 80 V/W falls short of the sensor manufactures claim of 193 V/W. This is due to differences in calibration procedures. The manufacturer calibrated under argon gas using a blackbody radiation source that heated the entire membrane surface while the model utilizes a small heat source that localizes the heat to a few micron area in the center of the membrane. When the manufacturer's methods were implemented in the model using our derived parameters, a sensitivity of 190 V/W was attained.

Device Optimization

Modeling revealed important information about our sensor that allowed us to find areas for improvement in its design. In an optimal device, S_{tot} must be maximized while C_{tot}, G_{tot}, and noise minimized. These parameters are determined by factors including the composition, thickness, and area of the membrane and thermopile, number of junctions, and sample droplet volume. Our current minimum sample volume of 2.5 nl is dictated by evaporative losses and sample delivery inaccuracy. Improvements in these areas could enable a minimum sample volume of 1 nl which would improve both τ and G_{tot} according to our model. Assuming a fixed sample volume of 1 nl it was then possible to find the optimal device dimensions and geometry.

At first glance an increase in the number of thermopile junctions through feature size reduction would seem to benefit Pmin by increasing S_{tot}; however any benefit is equally offset by an increase in noise. With the best amplifiers typically contributing at least 5 nV/√Hz noise[19] , it provides little benefit to reduce V_n past that level. It is more advantageous to keep V_n around 10 - 15 nV/√Hz so that amplifier noise is not a dominant factor. Therefore, calculations for Pmin were carried out with enough junctions to keep V_n in that range.

Since the membrane is the dominant factor in G_{tot}, using a membrane material with a lower Gmem, like a polymer, Pmin could be improved and at the same time the dependence on membrane thickness by Pmin is reduced (Figure 7C). The limiting factor is mechanical stability of the thin membranes, with 1 um being a realistic minimum thickness[20]. By using previously reported membranes like Su-8[21] or parylene-C[17], membrane heat flux could be reduced from 70% to 5% of G_{tot}. However, even with our current Gmem, higher sensitivities than previous studies [17]can be achieved due to our higher S_{tot}.

The Bi/Sb thermopiles used in our current device are ideal in terms of high Seebeck coefficient and low resistance. While optimizing the thermopile thickness we found that decreased thickness leads to reduce G_{tot} are at the expense of noise (Figure 7D). We selected the ideal thermopile thickness to be 1um for SiN membranes and 0.5 um for polymer membranes.

It is advantageous to have a large membrane area in order to reduce G_{tot}, however as membrane size increases, thermopile length also increases, resulting in an increased Johnson-Nyquist noise. Similarly, higher ΔT is realized at the thermopile junctions when they are situated centrally under the sample droplet, but this leads to more noise due to longer junctions and increases G_{tot} through conduction along the thermopile traces. By modeling a matrix of different sensing area widths (SA) and membrane widths (MW) using parameters from previous

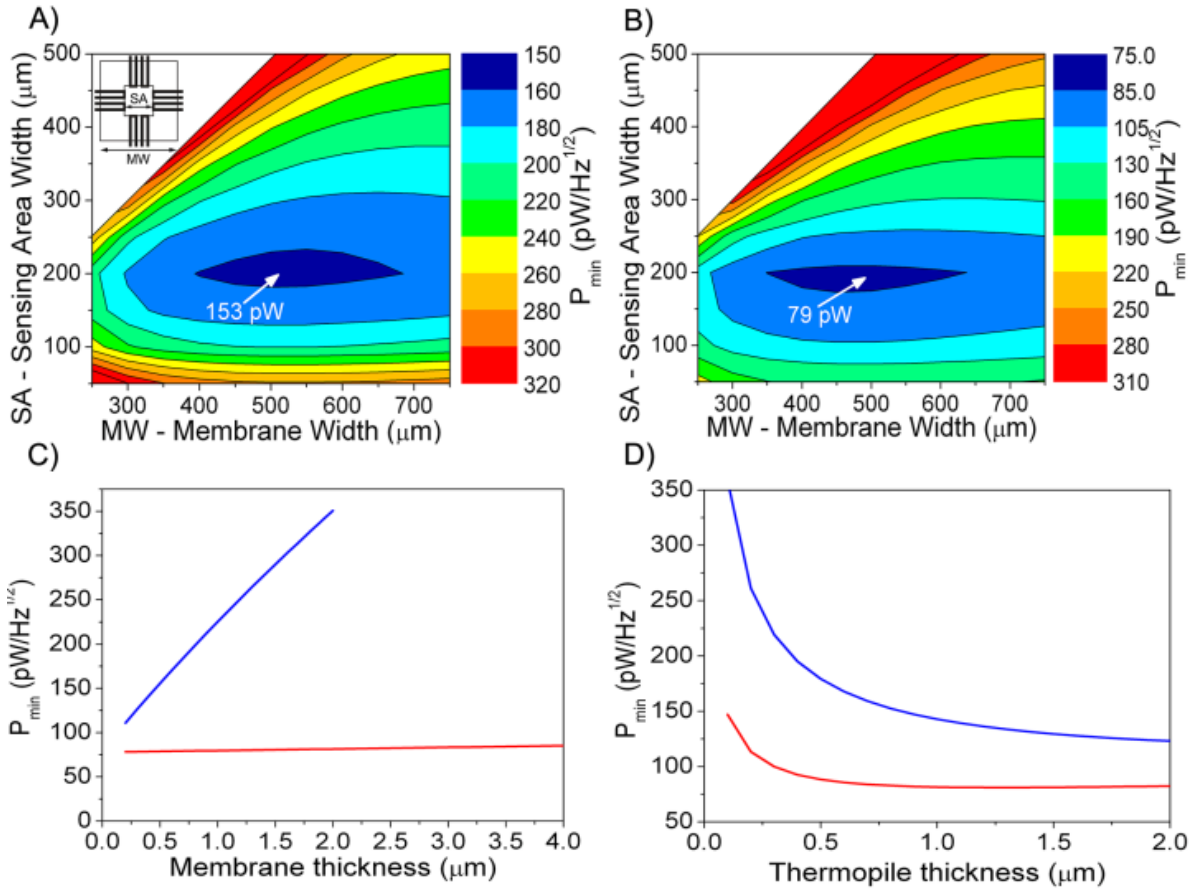

Figure 7. A) Contour plot showing how the minimum detectable energy changes as a function of membrane size and junction area for a 1 nl sample drop on a 1 μm SiN membrane. The best P_{min} is achieved at a membrane size of 500 μm and a junction size of 200 μm. **B)** Similar dimensions were found for a 1um thick polymer membrane, but with a lower resulting P_{min}. **C)** P_{min} is influenced much more by membrane thickness in SiN based (blue line) than polymer based (red line) calorimeters. **D)** Increasing thermopile thickness decreases noise (dotted line) and improves P_{min} for SiN (blue line) and polymer (red line) based calorimeter.

modeling, we found minima for both SiN and polymer membranes (Figures 7A-B). For both membranes, the optimal SA was ~200 um wide, placing the thermopile junctions just at the edge of a 1 nl droplet. This optimization also revealed the 2 fold improvement in Pmin by utilizing a polymer membrane over a SiN membrane (Figures 7A-B).

Error

A source of error in these reactions can be attributed to injection volume uncertainties. The PicoSpritzer II injection system used relies on air pressure and not on positive displacement to

deliver samples. At small (<100 pl) injection volumes, this results in short (<20 ms) injection pulses that are not far above the 3 ms air valve opening time. Random error determined experimentally with a series of injections is greatest at 2.5 nl base volume with a relative standard deviation of 2.3%, decreasing to 1.2% at 50 nl. Additional error is introduced at small volumes due to changes in the base drop volume. If the injection of reactants changes the base drop volume from 2.5 to 3.0 nl, sensitivity drops from 60.5 to 56.1 V/W, as shown in Figure 6 and in the decrease in peak amplitude seen in Figure 3. To attain sample volumes below 2.5 nl a more accurate injection system and better evaporation control is needed.

Determination of Time Constant

Time constant measurements of the system are higher than predicted by equation 4, but verified by the numerical model (Figure 8). Since τ was determined empirically by applying a 650 nm laser heating step function to the sensor with various volumes of water on it, little energy

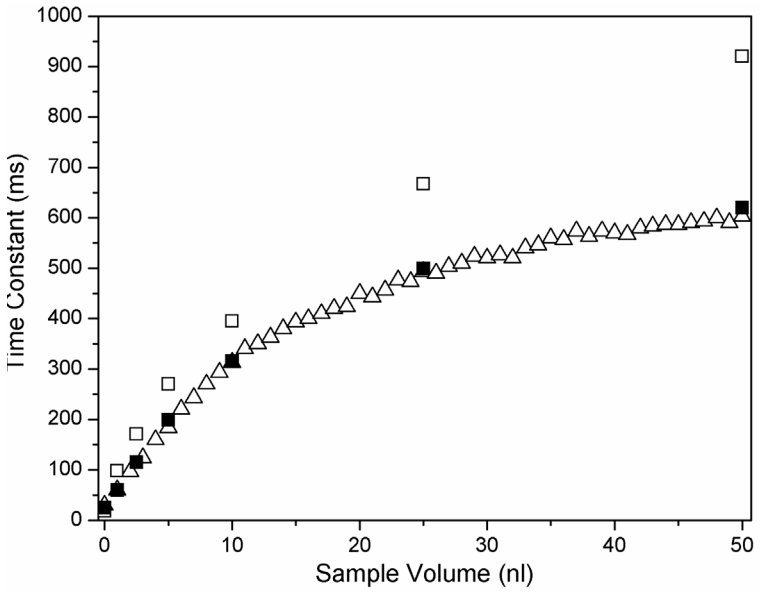

Figure 8. Time constant measured using a pulsed laser heat source at incrementally increased drop volumes (Δ) is matched well by the model data (■) and shows τ of 110 ms at 2.5 nl sample volume. However, when τ is calculated from C_{tot}/G_{tot} the results (□) are different due to localized drop heating.

was absorbed by the water drop. Most of the energy was deposited at the opaque SiN membrane surface, causing localized heating near the thermopiles. This causes an error in equation 4 since it assumes that the entire sample volume is heated uniformly. It also does not take into account differences in temperature distribution over the sample and membrane surfaces. When the model was changed from a point heat source to a constant heating throughout the sample, comparable time constants with the results from equation 4 were produced. The actual τ from a reaction on the calorimeter would be somewhere between the two findings. The laser heating results mimic what would occur in a chemical reaction where the reactants proceed to completion in a small volume of the total sample. The same would also be true in a biological assay where the cells would settle to the bottom of the sample drop. Even the worst case scenario of a τ of 170 ms for a 2.5 nl sample is still much better than other calorimeters with comparable sensitivity[17]. Theses finding also give more justification for utilizing smaller sample volumes in future calorimeter designs.

Minimum Detectable Energy

Pmin as predicted by equation 3 and shown in Figure 3 is 0.5 nW/√Hz at 2.5 nl and translates to a minimum power resolution of 1.5 nW/√Hz at a SNR of 3:1. Nanowatt resolution energy measurements were performed using our current calorimeter setup and achieved this level of sensitivity. When small droplets (12.5 pl – 800 pl) of dilute HCl were injected into a 2.5 nl drop of NaOH, as little as 1.4 nJ could be detected (Figure 9A). At 0.7 nJ, the peak was too small to be seen against the noise background. Injection artifacts were not seen until at least 100 pl of reactant was being injected (Figure 9B). The short time constant in conjunction with high sensitivity allows for the detection of these small, fast peaks that would be missed using other calorimeters.

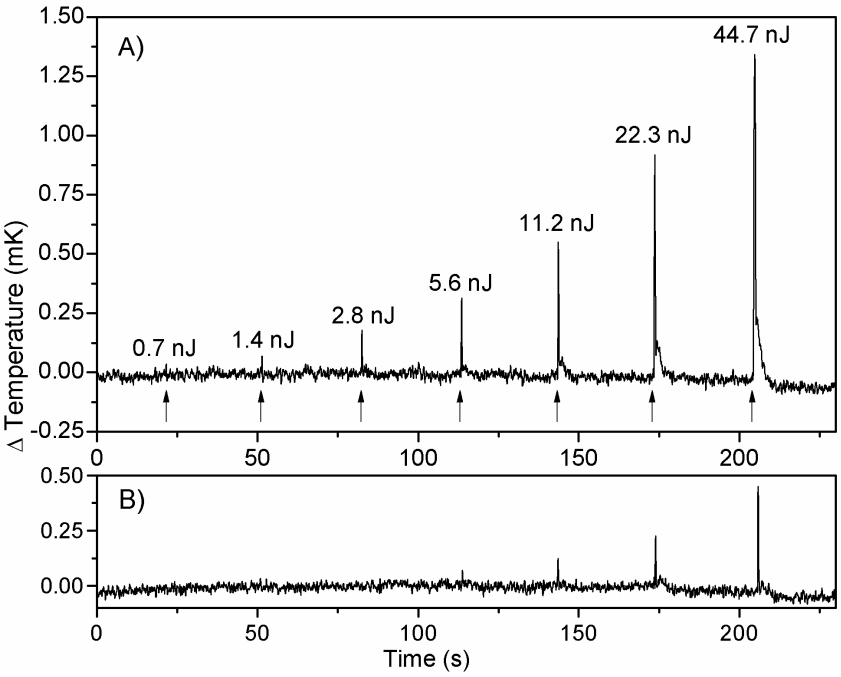

Figure 9. A) HCl injections into a 2.5 nl NaOH drop at each arrow showing the sub-nW capabilities of the sensor. **B)** Control injections of an equivalent volume of water into a 2.5 nl water drop.

Conclusions

We have described the use and optimization of a highly sensitive calorimeter which exceeds the capabilities of previously described calorimeters in both sensitivity and temporal response. Through reduction in sample volume and improvements in calibration, we showed, at 2.5 nl sample volume, a functional power resolution of 1.5 nW/√Hz and a sensitivity of 60 V/W, both an order of magnitude better than previously reported[5, 17, 20]. The reduction in sample volume also greatly enhanced τ, allowing for the first time sub-second measurements at high sensitivity. Modeling of the calorimeter allowed us to verify our results and determine if extending sample volumes smaller was warranted. Since only a 25% gain was predicted, we focused on using the model to design a calorimeter optimized for 1 nl samples. This showed the

possibility for a polymer based calorimeter with P_{min} of less than 100 pW/√Hz and τ of 160 ms. Sub-nanowatt sensitivities and short time constants are essential for monitoring dynamic non-equilibrium biomolecular processes with brief intermediate states like protein folding or cellular metabolism. Furthermore, these micromachined membrane based nanocalorimeters in combination with advanced electrowetting liquid handling techniques[22] could be operated in an array format required for combinatorial chemistry and drug discovery.

Acknowledgements

This work was supported in part by NIH Grant U01AI061223, the Vanderbilt Institute of Integrative Biosystems Research and Education (VIIBRE). We are especially indebted to Joseph Sun for his help in developing the finite element model. Furthermore we thank Joel Tellinghuisen and John Wikswo for helpful discussions.

References

1. Falconer, R.J.; Penkova, A.; Jelesarov, I.; Collins, B.M. *Survey of the year 2008: applications of isothermal titration calorimetry*. J. Mol. Recognit. 2010, 23 (5), 395-413.

2. Hansen, L.D.; Fellingham, G.W.; Russell, D.J. Simultaneous determination of equilibrium constants and enthalpy changes by titration calorimetry: Methods, instruments, and uncertainties. Anal. Biochem. 2011, 409 (2), 220-229.

3. Wiseman, T.; Williston, S.; Brandts, J.F.; Lin, L.N. *Rapid Measurement of Binding Constants and Heats of Binding Using A New Titration Calorimeter*. Anal. Biochem. 1989, 179 (1), 131-137.

4. Cooke, D.W.; Michel, K.; Hellman, F. Thermodynamic measurements of submilligram bulk samples using a membrane-based "calorimeter on a chip". Rev. Sci. Instrum. 2008, 79 (5), 053902.

5. Xu, J.; Reiserer, R.; Tellinghuisen, J.; Wikswo, J.P.; Baudenbacher, F.J. *A microfabricated nanocalorimeter: design, characterization, and chemical calibration.* Anal. Chem. 2008, 80 (8), 2728-2733.

6. Roselin, L.; Lin, M.S.; Lin, P.H.; Chang, Y.; Chen, W.Y. *Recent trends and some applications of isothermal titration calorimetry in biotechnology*. Biotechnol. J. 2010, 5 (1), 85-98.

7. Ball, V.; Maechling, C. *Isothermal Microcalorimetry to Investigate Non Specific Interactions in Biophysical Chemistry*. International Journal of Molecular Sciences 2009, 10 (8), 3283-3315.

8. Carreto-Vazquez, V.H.; Liu, Y.S.; Bukur, D.B.; Mannan, M. *Chip-scale calorimeters: Potential uses in chemical engineering.* J. Loss Prev. Process Indust. 2011, 24 (1), 34-42.

9. Ferenczy, G.G.; Keserue, G.M. *Thermodynamics guided lead discovery and optimization*. Drug Discov. Today 2010, 15 (21-22), 919-932.

10. Manta, B.; Obal, G.; Ricciardi, A.; Pritsch, O.; Denicola, *A. Tools to evaluate the conformation of protein products*. Biotechnol. J. 2011, 6 (6), 731-741.

11. Vine, G.J.; Bishop, A.H. The analysis of microorganisms by microcalorimetry in the pharmaceutical industry. Curr. Pharm. Biotechnol. 2005, 6 (3), 223-238.

12. Khan, S.H.; Ahmad, F.; Ahmad, N.; Flynn, D.C.; Kumar, R. *Protein-Protein Interactions: Principles, Techniques, and their Potential Role in New Drug Development*. J. Biomol. Struct. Dyn. 2011, 28 (6), 929-938.

13. Verhaegen, K.; Baert, K.; Simaels, J.; Van Driessche, W. *A high-throughput silicon microphysiometer*. Sensors and Actuators a-Physical 2000, 82 (1-3), 186-190.

14. Wadso, I.; Wadso, L. *Systematic errors in isothermal micro- and nanocalorimetry*. J. Therm. Anal. Calorim. 2005, 82 (3), 553-558.

15. Boyer, A.; Cisse, E. *Properties of Thin-Film Thermoelectric-Materials - Application to Sensors Using the Seebeck Effect*. Materials Science and Engineering B-Solid State Materials for Advanced Technology 1992, 13 (2), 103-111.

16. Bourque-Viens, A.; Aimez, V.; Taberner, A.; Nielsen, P.; Charette, P.G. *Modelling and experimental validation of thin-film effects in thermopile-based microscale calorimeters*. Sensors and Actuators a-Physical 2009, 150 (2), 199-206.

17. Lee, W.; Fon, W.; Axelrod, B.W.; Roukes, M.L. *High-sensitivity microfluidic calorimeters for biological and chemical applications*. Proc. Natl. Acad. Sci. U. S. A. 2009, 106 (36), 15225-15230.

18. Briggner, L.E.; Wadso, I. Test and calibration processes for microcalorimeters, with special reference to heat conduction instruments used with aqueous systems. J. Biochem. Biophys. Methods 1991, 22 (2), 101-118.

19. Klushin, A.M.; Komkov, A.V.; Gelikonova, V.D.; Borovitskii, S.I.; Siegel, M. *DC voltage calibrator based on an array of high-temperature superconductor Josephson junctions*. IEEE Transactions on Instrumentation and Measurement 2003, 52 (2), 529-532.

20. Johannessen, E.A.; Weaver, J.M.; Cobbold, P.H.; Cooper, J.M. *A suspended membrane nanocalorimeter for ultralow volume bioanalysis.* IEEE Trans Nanobioscience 2002, 1 (1), 29-36.

21. Mattsson, C.G.; Thungstrom, G.; Bertilsson, K.; Nilsson, H.-E.; Martin, H. *Development of an infrared thermopile detector with a thin self-supporting SU-8 membrane*. In IEEE Sensors 2007, Atlanta, GA, 2007.

22. Wheeler, A.R.; Moon, H.; Kim, C.J.; Loo, J.A.; Garrell, R.L. Electrowetting-based microfluidics for analysis of peptides and proteins by matrix-assisted laser desorption/ionization mass spectrometry. Anal. Chem. 2004, 76 (16), 4833-4838.

CHAPTER III

CONCLUSIONS AND FUTURE WORK

Conclusions

We have shown that nanowatt power resolution can be achieved using off-the-shelf IR sensors adapted to calorimetry. We successfully characterized the devices and showed that they can be used to measure small, fast reactions in as little as 2.5 nl volume. With 1.4 nJ power resolution and 110 ms τ, the door to single-cell energy measurements is opened. The combined power sensitivity and τ of our device exceeds that of any other published calorimeter: we have achieved this performance by utilizing a high S_{tot} and pushing the sample volume smaller. Computer modeling of the devices allowed us to verify our findings and explain measurement artifacts encountered during the study. This model also showed that a new generation of calorimeter could be built with a power resolution of less than 100 pW while still maintaining a fast τ.

Future Work

Using our off-the-shelf calorimeter, we are beginning experiments are to measure the energy associated with bovine adrenal chromaffin cell catecholamine release in conjunction with microelectrode recording techniques. The goal is to quantitate the energy required during neurotransmitter release and couple that to alterations in the normal endocytosis cycle. Work is

also underway to measure the energy of single contractions from individual, electrically stimulated murine cardiomyocytes. This work is to support findings on altered metabolic states in hypertrophic cardiomyopathy. A future project aims to measure contraction energy from whole, embryonic zebrafish hearts

In order to realize 1 nl working sample volumes, we need to improve our liquid handling need to be made. Test are currently underway with electrowetting on dielectric (EWOD) devices that allow sample drops to be controlled electronically without the use of pipets or microfluidic channels. The use of EWOD technology would be essential for any large scale array usage of calorimeters and would eliminate some of the artifacts seen during pipette injections. Other work is underway to construct the optimized calorimeter devices using microfabrication and photolithographic techniques in the VIIBRE labs**.**

APPENDIX A

LABVIEW SIGNAL RECORDER AND INJECTION CONTROL

Labview Front Panel

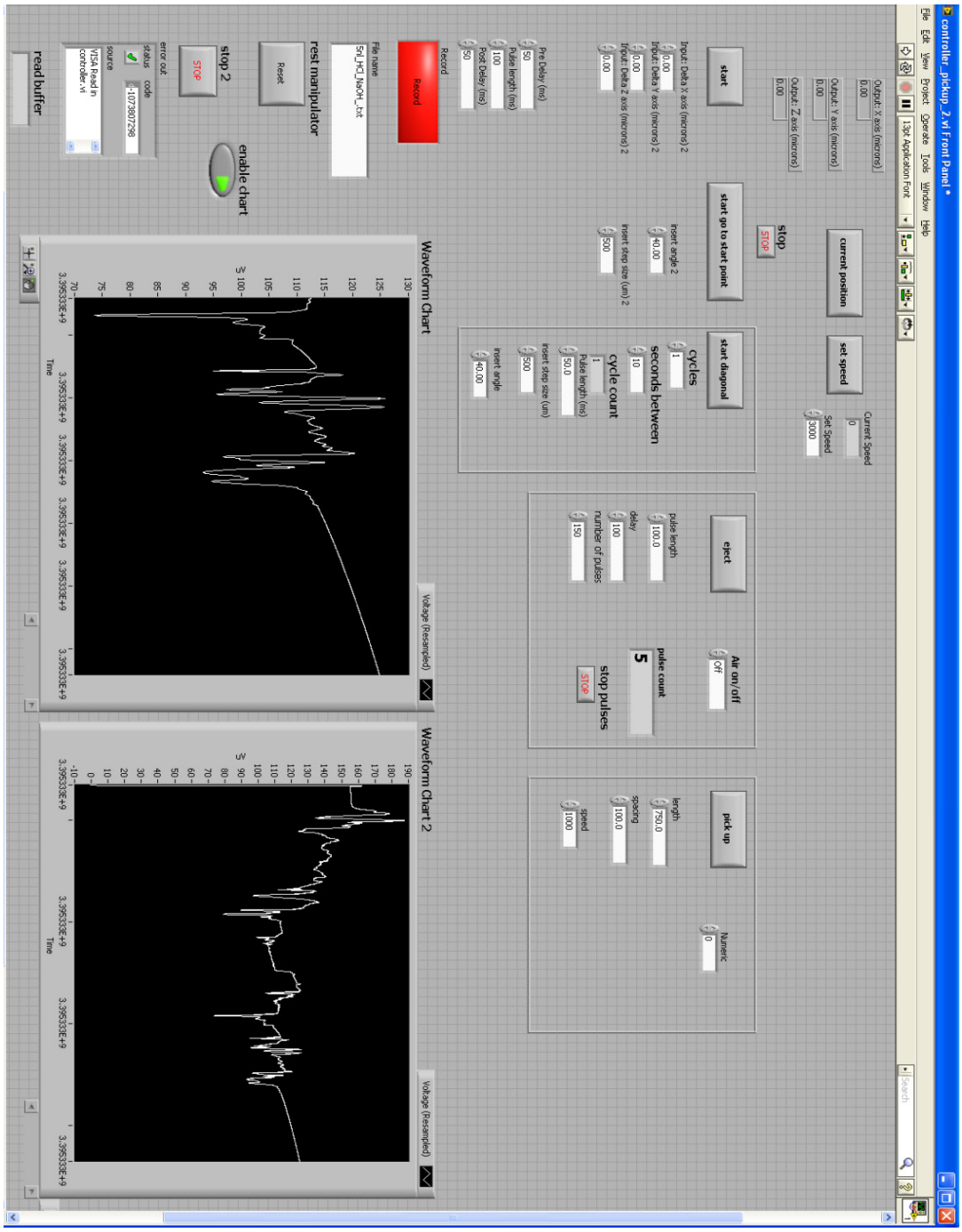

Block Diagram

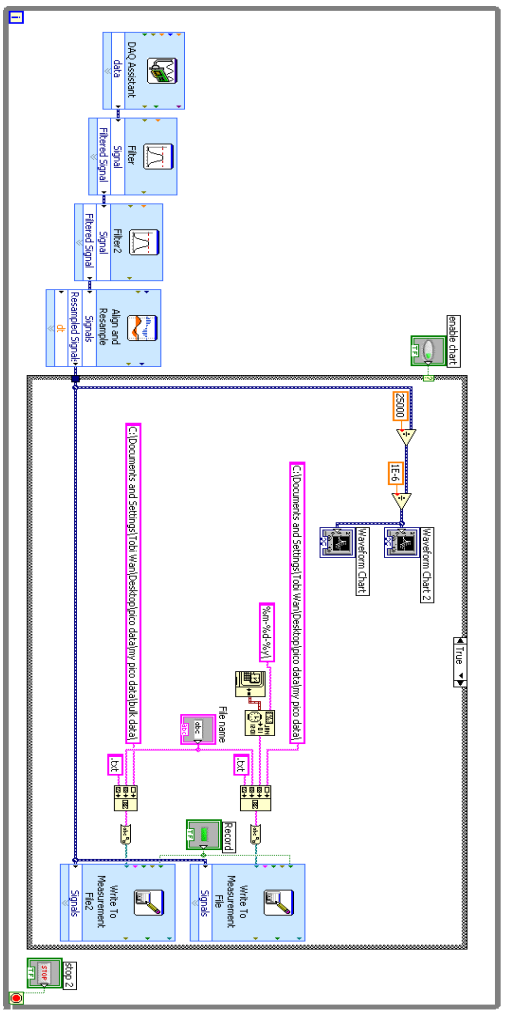

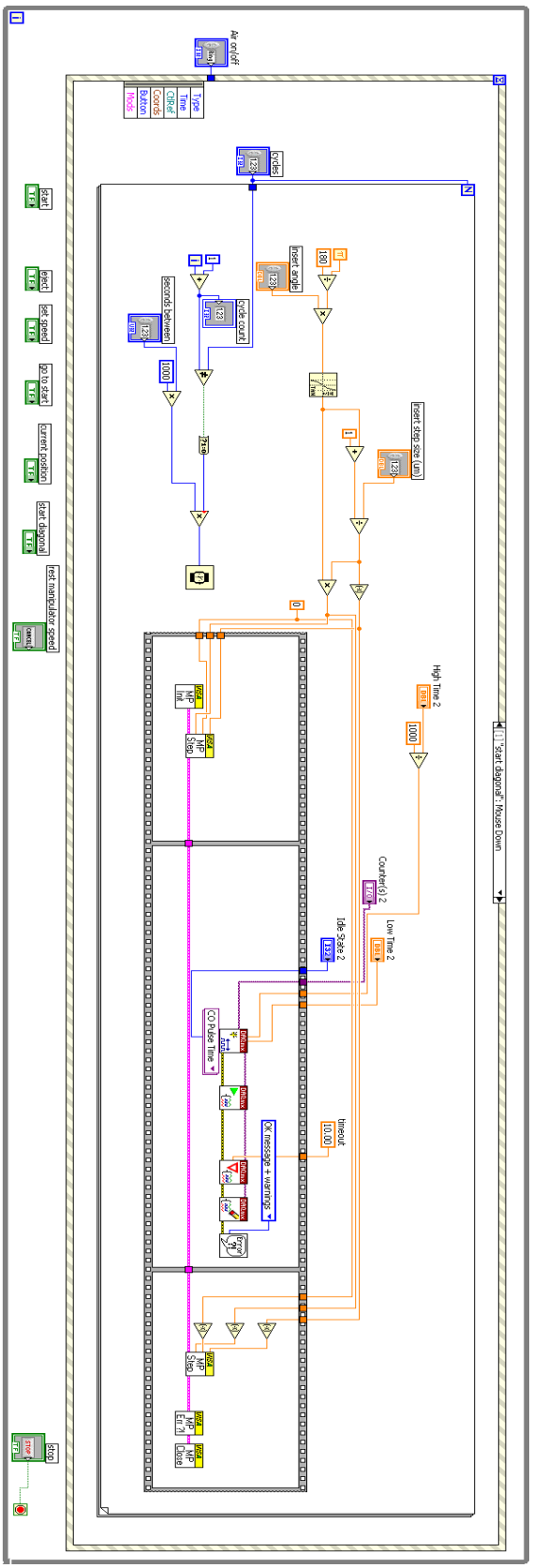

APPENDIX B

MATLAB SIGNAL PROCESSING M CODE

heat_equations.m

```
%Calculates heat of neutralization and corrects for concentration,
%dilution curves and equations derived from: Parker, V.B., Thermal Properties of Aqueous
Univalent Electrolytes, National Bureau of Standards #2, 1965.
clear all
close all
clc

m=0.001:0.001:1;

i=round(m*1000);
M=18.01528;
mp=55.51.*m./(111.02+m);
ip=round(mp*1000);
ip(1)=1;
% NaOH
load -mat NaOH_fit  %NaOH heat of dilution curve, converted from molality to molarity.
l1_B=-((M.*m.^2)./1000);
ll1_B=transpose(differentiate(NaOH_fit,m));
L1_B=l1_B.*ll1_B;
l2_B=transpose(NaOH_fit(m));
ll2_B=(55.51./m).*L1_B;
L2_B=l2_B-ll2_B;

%HCl heat of dilution curve
load -mat HCl_fit
l1_A=-((M.*m.^2)./1000);
ll1_A=transpose(differentiate(HCl_fit,m));
L1_A=l1_A.*ll1_A;
l2_A=transpose(HCl_fit(m));
ll2_A=(55.51./m).*L1_A;
L2_A=l2_A-ll2_A;

%NaCl heat of dilution curve
```

```
load -mat NaCL_fit
l1_S=-((M.*m.^2)./1000);
ll1_S=transpose(differentiate(NaCl_fit,m));
L1_S=l1_S.*ll1_S;
l2_S=transpose(NaCl_fit(m));
ll2_S=(55.51./m).*L1_S;
L2_S=l2_S-ll2_S;
figure(1)
hold on
plot(NaCl_fit,'-b')
plot(HCl_fit,'-g')
plot(NaOH_fit,'-r')

figure(2)
hold on
grid on
plot(m,L1_S,m,L1_A,m,L1_B)
figure(3)
hold on
grid on
plot(m,L2_S,m,L2_A,m,L2_B)

% heat eq
h1=-55835+(L2_S(ip)-L2_B(i)-L2_A(i));
h2=55.51./m;
h3=(m./mp).*L1_S(ip);
h4=-L1_B(i)-L1_A(i);
HD=h1+(h2.*(h3+h4));
figure(4)
plot(m,-HD)
title('Heat per mol of injected acid or base')
grid on

%% Calculates energy
%under equimolar conditions injecting NaOH or HCl gives same energy.
clc

% injected volume (l)
Vi=100e-9;
% injected concentration (M)
Xi=0.001;
HDindex=Xi*1000;
J_per_M=HD(HDindex);
Ji=Vi.*(J_per_M*Xi) %expected energy for each injection
```

deconvolve.m

```
%Raw data from recordings of acid-base injections are detrended, deconvolved from
%baseline shift, and power sensitivity is calculated at each injection.
clear all
close all
clc

Data1=dlmread('_.txt','\t'); %Raw data recorded in LabView
Data=Data1(:,2);
N=length(Data);
figure(1);grid on;
f=100;     % frequency
G=25000;    %gain
p=10;       % # peaks to consider
E=1e-8;   %energy per injection, from heat_equations.m
Start_point=1*f;    %set start of data
End_point=1000*f;    %set end of data
R=-2.5;        % retrend, used to flatten baseline


Data_1= Data(Start_point:End_point)/G*1e6; %convert from V to uV
Data_2=detrend(Data_1);
N_2=length(Data_2);
S1=1;
S2=N_2;
figure (1)
plot(Data_2(S1:S2));
title('Detrended data')
ylabel('uV')
grid on

y=1:length(Data_2);
trend=y'*-1e-6*R;
Data_2=Data_2+(trend*-12); %Add slight trend back to data to make baseline detection work
better

figure(2)
plot(Data_2)
title('Retrended Data')
ylabel('uV')
grid on
```

```
Max_point=zeros(2000,2); % this array will be used to store the peak values of the data
j=1;
for i=2:(N_2-1)
   if Data_2(i)>-.1 % peak heights to include, only peaks larger than this considered
      Max_point(j,1)=i;Max_point(j,2)=Data_2(i);
      j=j+1;
   end
end
j=j-1;
figure(3)
plot(Max_point(1:j,1),Max_point(1:j,2));
title('Peaks')
Peak=zeros(p,1); % this array to store the peak values
Mark_1=1;Mark_2=0;
%these two variables will be used to store the local limit for one injection
k=1;
q=0;
for i=1:j
   if Max_point(i+1,1)-Max_point(i,1)>2000 %only selects peaks spaced at least 20s apart
      Mark_2=i;
      [Y,I] = max(Max_point(Mark_1:Mark_2,2));
      Peak(k)=Max_point(I+q,1);
      Mark_1=i+1;
      k=k+1;
      q=i;
   end
end
[Y,I] = max(Max_point(Mark_1:i,2)); %catches last peak missed by loop
Peak(k)=Max_point(I+q,1);

Voltage_time=zeros(p,1); %this array to record the voltage*time for each injection
base=zeros(2000,1);
baseline=zeros(p,1);
baselinea=zeros(p,1);
offset=zeros(p,1);
for i=1:p
    baselinea(i)=mean(Data_2(Peak(i)+1500:Peak(i)+2000));
    baseline(i)=mean(Data_2(Peak(i)-500:Peak(i)-25));
    offset(i)=baseline(i)-baselinea(i); %find baseline shift
    Data_2(Peak(i)-25:N_2)=Data_2(Peak(i)-25:N_2)+offset(i); %remove baseline shift
end

for i=1:p
   baselinea(i)=mean(Data_2(Peak(i)-400:Peak(i)-50));
```

```
   for k=1:550
      q=(Data_2(Peak(i)-50+k)-baselinea(i))*(1/f);
      Voltage_time(i)=Voltage_time(i)+q;  %uV/s for each injection
   end
end

figure(4)
plot(Data_2)
grid on

figure(5)
plot(Voltage_time)
title('Voltage time')

Voltage_time
scaledVT = Voltage_time./1e6;    %convert back to V/s

VperW=scaledVT./E   %sensitivty in volts per watt for each injection
VperWavg=mean(VperW)
deviation_pct=std(VperW)/VperWavg*100

figure(6)
plot(VperW)
```

APPENDIX C

COMSOL FITTING AND OPTIMIZATION M CODE

run_fitting_5nl.m

```
%Run Comsol fitting to find material parameters such that experimental data
%and Comsol output match. Membrane conductivity and origin of heat source in
%sample drop varied to find best fit.
close all
clear all
clc

X0=[15;2.5;];   %Starting parameters for membrane conductivity, origin of heat source in
sample drop.
xdata=0:0.01:1.99;  %time base for data
load('fivenlcurve.mat');    %Fitting to 5nl acid-base injections, ydata
LB=[0;0];
UB=[50;20];
options = optimset('Tolfun',1e-6,'TolX',1e-6,'Display','iter','DiffMinChange',0.01,...
   'DiffMaxChange',1,'FinDiffType','central');
M=lsqcurvefit('comsol',X0,xdata,ydata,LB,UB,options)    %Perform least squares non-linear
curve fitting of Comsol model to experimental data such that the shape and time course of each
match.
%Stot calculated based on scaling difference between experimental and model
%data once peak shape fit.
plot(xdata,ydata,xdata,peak,'-g')
```

comsol.m

```
function output=comsol(x,xdata)
% Comsol backbone function for run_fitting_5nl.m
% COMSOL Multiphysics Model M-file
% Generated by COMSOL 3.5a RC1 (COMSOL 3.5.0.595, $Date: 2008/11/24 17:02:12 $)
K=x(1) %membrane conductivity
D=x(2) %heat source placement above membrane (0=touching)
flclear fem

% COMSOL version
clear vrsn
vrsn.name = 'COMSOL 3.5';
vrsn.ext = 'a RC1';
vrsn.major = 0;
vrsn.build = 595;
vrsn.rcs = '$Name:  $';
vrsn.date = '$Date: 2008/11/24 17:02:12 $';
fem.version = vrsn;

flbinaryfile='five_minimala.mphm';

% Geometry
clear draw
g18=flbinary('g18','draw',flbinaryfile);
draw.p.objs = {g18};
draw.p.name = {'PT1'};
draw.p.tags = {'g18'};
g1=flbinary('g1','draw',flbinaryfile);
g10=flbinary('g10','draw',flbinaryfile);
g11=flbinary('g11','draw',flbinaryfile);
g12=flbinary('g12','draw',flbinaryfile);
g13=flbinary('g13','draw',flbinaryfile);
g2=flbinary('g2','draw',flbinaryfile);
g3=flbinary('g3','draw',flbinaryfile);
g4=flbinary('g4','draw',flbinaryfile);
g5=flbinary('g5','draw',flbinaryfile);
g6=flbinary('g6','draw',flbinaryfile);
g7=flbinary('g7','draw',flbinaryfile);
g8=flbinary('g8','draw',flbinaryfile);
g9=flbinary('g9','draw',flbinaryfile);
```

```
draw.s.objs = {g1,g10,g11,g12,g13,g2,g3,g4,g5,g6,g7,g8,g9};
draw.s.name = {'CO1','CO10','CO11','CO12','CO13','CO2','CO3','CO4','CO5','CO6', ...
 'CO7','CO8','CO9'};
draw.s.tags = {'g1','g10','g11','g12','g13','g2','g3','g4','g5','g6','g7','g8', ...
 'g9'};
fem.draw = draw;
fem.geom = flbinary('g19','geom',flbinaryfile);

% Geometry
g9=move(g9,[0,-35e-6]);
g9=move(g9,[0,D*1e-6]); %droplet placement
gg=geomedit(g18);
gg{1}=point2(-30E-6,-1.0E-6);   %T measure point
g20=geomedit(g18,gg);

% Analyzed geometry
clear p s
p.objs={g20};
p.name={'PT1'};
p.tags={'g20'};

s.objs={g1,g2,g3,g4,g5,g6,g7,g8,g9,g10,g11,g12,g13};
s.name={'CO1','CO2','CO3','CO4','CO5','CO6','CO7','CO8','CO9','CO10', ...
 'CO11','CO12','CO13'};
s.tags={'g1','g2','g3','g4','g5','g6','g7','g8','g9','g10','g11', ...
 'g12','g13'};

fem.draw=struct('p',p,'s',s);
fem.geom=geomcsg(fem);

% Initialize mesh
fem.mesh=meshinit(fem, ...
            'hauto',6);

% (Default values are not included)

% Application mode 1
clear appl
appl.mode.class = 'HeatTransfer';
appl.mode.type = 'axi';
appl.border = 'on';
appl.assignsuffix = '_ht';
clear bnd
bnd.name = {'temp','cont','axial'};
```

```
bnd.type = {'q0','cont','ax'};
bnd.T0 = 0;
bnd.ind = [1,1,1,2,2,2,2,2,2,2,2,2,2,2,2,2,2,2,2,2,2,2,2,2,2,2,2,2,2,2,2, ...
  3,3,3,3,3,3,3,3,3,3,3,3,2,2,2,2];
appl.bnd = bnd;
clear equ
equ.C = {1000,750,1966,700,750,4050,4050};
equ.init = 0;
equ.k = {0.024,1,0.13,149,1,0.058,0.058};
equ.Q = {0,0,0,0,0,0,'2.83e7*(t>0.1)*(t<0.2)'};
equ.name = {'air','glass','oil','si','mem','water',''};
equ.rho = {1.2,2200,830,2300,2700,1000,1000};
equ.ind = [1,2,2,2,2,2,3,1,4,5,1,6,7];
appl.equ = equ;
fem.appl{1} = appl;
fem.sdim = {'r','z'};
fem.frame = {'ref'};
fem.border = 1;
fem.outform = 'general';
clear units;
units.basesystem = 'SI';
fem.units = units;

% ODE Settings
clear ode
clear units;
units.basesystem = 'SI';
ode.units = units;
fem.ode=ode;

% Multiphysics
fem=multiphysics(fem);

% Extend mesh
fem.xmesh=meshextend(fem);

% Solve problem
fem.sol=femtime(fem, ...
            'solcomp',{'T'}, ...
            'outcomp',{'T'}, ...
            'blocksize','auto', ...
            'tlist',[colon(0,0.01,2)], ...
            'tout','tlist', ...
            'atol',{'0.001'}, ...
```

```
            'maxstep',0.01);

% Save current fem structure for restart purposes
fem0=fem;



% Integrate
peak=postint(fem,'T', ...
        'unit','K', ...
        'recover','off', ...
        'dl',22, ...
        'edim',0, ...
        'solnum',1:200);
load('fivenlcurve.mat');
k=0;
while 1<2
   [y,I]=max(peak);
   [yd,Id]=max(ydata);
   if I<Id
      peak=[0 peak];
      peak(201)=[];
      k=k+1;
   end
   if I>Id
      peak(1)=[];
      peak(200)=peak(199);
      k=k-1;
   end
   if I==Id
      break
   end
end
offset=k
seebeck=mean(peak)/mean(ydata)
output=peak./seebeck;
```

run_optimization_poly.m

```
%Run Comsol optimization to find the optimal calorimeter dimensions,
%calculates minimum detectable energy in a 1 nl sample drop based on
%changes in Vn, Gtot, and Stot.  Comsol runtime preloaded with material properties and
starting dimensions.
close all
clear all
clc

p1=1290e-9; %Bi rho
p2=417e-9;  %Sb rho
tp=1e-6;  %thermopile thickness, in this case polymer membrane parameters are loaded into
Comsol
S=150e-6;   % Seebeck coefficient
Kb=1.38e-23;
T=300;

Q=100e6;
x=(249:50:499)'*1e-6;   %aa size, width of sensing area junctions
y=(250:50:500)'*1e-6;  %mem diameter, width of free standing membrane
%as x and y are varied that thermopile track length changes so Vn changes.
%Additionally, the changing membrane size affects Gtot

for d=1:length(y)
   for aa=1:length(x)
      if x(aa)<y(d)
         tic
         Gtot(d,aa)=comsol1nlpoly(Q,y(d),x(aa)) %Comsol runtime called and each size processed
         J=(x(aa)/20e-6)*4;
         noise(d,aa)=sqrt(4*Kb*T*(((p1+p2)/2)*(2*J*((y(d)-x(aa)+50e-6)/2))/(tp*5e-6)));
         nstar(d,aa)=sqrt(4*Kb*T*(((p1+p2)/2)*((x(aa)*(y(d)-x(aa)+50e-6))/(tp))))/((x(aa)*150e-
6));
         Pmin(d,aa)=nstar(d,aa)*Gtot(d,aa);
         toc
      else
         Pmin(d,aa)=NaN;
         Gtot(d,aa)=NaN;
         noise(d,aa)=NaN;
      end
   end
end
figure(1)
```

```
surf(y,x,Pmin')
hold on
title('Pmin')
axis([min(y) max(y) min(x) max(x) 0 200e-12])
contour(y,x,Pmin')
shading interp
colorbar

figure(2)
surf(y,x,Gtot') %Heat flow, W/mK
hold on
title('Gtot')
axis([min(y) max(y) min(x) max(x) 0 400e-6])
contour(y,x,Gtot')
shading interp
colorbar

figure(3)
surf(y,x,noise')
hold on
title('Noise')  %Total Johnson noise
axis([min(y) max(y) min(x) max(x) 0 10e-9])
contour(y,x,noise')
shading interp
colorbar
```